PHYSICAL REVIEW B **80**, 174502 (2009)

Power-dependent internal loss in Josephson bifurcation amplifiers

Michio Watanabe,[1,*] Kunihiro Inomata,[1] Tsuyoshi Yamamoto,[1,2] and Jaw-Shen Tsai[1,2]
[1]*RIKEN Advanced Science Institute, 34 Miyukigaoka, Tsukuba, Ibaraki 305-8501, Japan*
[2]*NEC Nano Electronics Research Laboratories, 34 Miyukigaoka, Tsukuba, Ibaraki 305-8501, Japan*
(Received 5 June 2009; revised manuscript received 12 August 2009; published 3 November 2009)

We have studied nonlinear superconducting resonators: $\lambda/2$ coplanar-waveguide (CPW) resonators with Josephson junctions (JJs) placed in the middle and $\lambda/4$ CPW resonators terminated by JJs, which can be used for the qubit readout as "bifurcation amplifiers." The nonlinearity of the resonators arises from the Josephson junctions, and because of the nonlinearity, the resonators with appropriate parameters are expected to show a hysteretic response to the frequency sweep, or "bifurcation," when they are driven with a sufficiently large power. We designed and fabricated resonators whose resonant frequencies were around 10 GHz. We characterized the resonators at low temperatures, $T < 0.05$ K, and confirmed that they indeed exhibited hysteresis. The sizes of the hysteresis, however, are sometimes considerably smaller than the predictions based on the loaded quality factor in the weak drive regime. When the discrepancy appears, it is mostly explained by taking into account the internal loss, which often increases in our resonators with increasing drive power in the relevant power range. As a possible origin of the power-dependent loss, the quasiparticle channel of conductance of the JJs is discussed.

DOI: 10.1103/PhysRevB.80.174502 PACS number(s): 84.40.−x, 74.50.+r, 85.25.Cp

I. INTRODUCTION

In many experiments related to quantum information processing, the readout plays a critical role. One of the recent major steps forward in the experiments of superconducting qubits was related to the improvement of readout and the quantum nondemolition readout was reported.[1] In the readout scheme of Ref. 1, the charge qubit was nonresonantly coupled to a superconducting linear resonator. The qubit state was detected as a shift in the resonant frequency of the resonator. The measurements were done with a weak driving power of $n \sim 1$, where n is the number of measurement photons populated in the resonator.

It has been suggested that employing a nonlinear resonator instead of linear resonator should relax the strong demand of low-noise broadband microwave measurements because the latching effect between the bistable states in a nonlinear resonator is expected to provide a larger but still fast enough response.[2] Such scheme, or the "bifurcation amplifier," has been applied to the readout of charge qubits[3–5] and flux qubits,[6–9] where Josephson junctions (JJs) as nonlinear inductors are employed for the nonlinear resonators. In many cases, the nonlinear resonators with JJs have lumped-element capacitors and their resonant frequencies are around 1 GHz.[3,4,6,8,9] In general, however, using a distributed element such as a coplanar waveguide (CPW) (Refs. 5 and 10–12) makes it easier to increase the resonant frequency and the quality factor. A higher resonant frequency is advantageous for suppressing photon-number fluctuations, which may cause qubit dephasing even when the readout circuit is turned off.[13] Choosing a high-quality factor and a resonant frequency much higher than the qubit frequency would be also helpful in suppressing the qubit relaxation through the resonator.[14]

In this work, we have characterized at low temperatures, $T < 0.05$ K, nonlinear CPW resonators with JJs, whose resonant frequencies are as high as 10–11 GHz. We observed the "bifurcation" as expected theoretically; the resonators showed a hysteretic response to the frequency sweep when they were driven with a sufficiently large power. We analyze the hysteresis in detail, paying close attention to the internal loss, which has not necessarily been examined well in the earlier works[8,10] on superconducting nonlinear resonators designed for reading out flux and charge qubits.

II. THEORY

The nonlinear resonators studied in this work are shown schematically in Figs. 1(a) and 1(b). They are $\lambda/2$ and $\lambda/4$ CPW resonators, respectively. The crosses in the figures denote either single JJs or dc superconducting quantum interference devices (SQUIDs), the origin of the nonlinearity. We

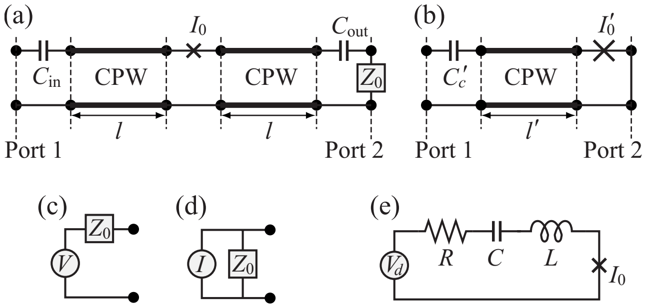

FIG. 1. Schematic diagrams of microwave circuits. (a) $\lambda/2$ and (b) $\lambda/4$ CPW resonators with JJs, where I_0 and I_0' are the critical currents of the junctions, l and l' are the CPW length, and $C_{\rm in}$, $C_{\rm out}$, and C_c' are the coupling capacitance to the microwave line. Both in (a) and (b), Port 1 is connected to a microwave source, which can be expressed as (c) an ideal voltage source and $Z_0 = 50\ \Omega$ in series, or (d) an ideal current source and Z_0 in parallel. Port 2 is terminated by Z_0 in (a), whereas shorted in (b). In the vicinity of the resonance, (a) has been mapped to (e) a series circuit of LCR and JJ (Refs. 10 and 11).

©2009 The American Physical Society

treat dc SQUIDs as single JJs with tunable critical currents I_0. Here, we should mention that superconducting transmission lines can also exhibit nonlinearity.[15–17] The microwave power required for this effect, however, is many orders of magnitude larger than the power range of our experiments. Thus, we treat superconducting CPWs as linear elements. Port 1 in Figs. 1(a) and 1(b) is connected to a microwave source, whose equivalent circuits are Figs. 1(c) and 1(d). For uniformity, we always use Fig. 1(c) in this paper. The $\lambda/2$ resonator in Fig. 1(a) has been mapped[10,11] to a series circuit of *LCR* and JJ [see Fig. 1(e)] in the vicinity of the resonance, by considering the electromagnetic environment seen from the JJ in the linear regime, where the drive is so weak that the resonator does not manifest nonlinearity. The series circuit is one of the nonlinear systems studied by Manucharyan *et al.*[18] They solved the equation for the Duffing oscillator by retaining the terms with the first harmonic only, then, mapped several nonlinear systems to the Duffing oscillator by comparing the differential equations of the systems with the Duffing equation.[18]

The series resonant circuit in Fig. 1(e) "bifurcates" and becomes bistable in a certain frequency range when the drive amplitude V_d exceeds a critical value V_c, provided that the amplitude I_c of the current through JJ at $V_d = V_c$ is sufficiently smaller than I_0. According to Ref. 18,

$$V_c = \frac{8}{3^{3/4}}\left(\frac{1}{Q_l}\frac{L}{L_{J0}}\right)^{3/2}\omega_c\varphi_0 \tag{1}$$

and

$$I_c/I_0 = \frac{4}{3^{1/4}}\left(\frac{1}{Q_l}\frac{L}{L_{J0}}\right)^{1/2}, \tag{2}$$

where

$$Q_l = (Q_e^{-1} + Q_u^{-1})^{-1} \tag{3}$$

is the loaded quality factor, Q_e is the external quality factor, Q_u is the unloaded quality factor,

$$L_{J0} = \varphi_0/I_0 \tag{4}$$

is the Josephson inductance, $\varphi_0 = \hbar/(2e)$, ω_c satisfies

$$\Omega_c \equiv 2Q_l(1 - \omega_c/\omega_0) = \sqrt{3}, \tag{5}$$

and ω_0 is the resonant angular frequency in the linear regime. Equations (2) and (4) suggest that a large Q_l and a small I_0 are favorable for the bifurcation. When $Q_l \gg 1$, the normalized boundaries of the bistable region are expressed as

$$\frac{V(\Omega)}{V_c} = \frac{1}{2}\frac{\Omega^{3/2}}{\Omega_c^{3/2}}\left[1 + 3\frac{\Omega_c^2}{\Omega^2} \pm \left(1 - \frac{\Omega_c^2}{\Omega^2}\right)^{3/2}\right]^{1/2}, \tag{6}$$

where $\Omega = 2Q_l(1-\omega/\omega_0)$ and ω is the angular frequency.[18]

The mapping[10,11] of Fig. 1(a) to Fig. 1(e) has been done for circuits with $L \gg L_{J0}$ by assuming that

$$V_d = Z_0\omega_0 C_{\text{in}} V, \tag{7}$$

where $Z_0 = 50\ \Omega$ and C_{in} is the coupling capacitance to the input microwave line, and that

$$L + L_{J0} \sim L = \pi Z_0/(2\omega_0). \tag{8}$$

Note that the mapping is based on the behavior in the linear regime. We have simulated the circuit in Fig. 1(a) taking into account the drive-strength dependence, as we will describe in the next paragraphs, and confirmed that the simulated V_c and the value calculated from Eqs. (1), (7), and (8) agree reasonably well.

The heart of our simulation is expressing JJ as an inductance that depends on the amplitude Δ of the superconducting-phase oscillation,

$$L_J(\Delta) = \frac{\Delta}{2J_1(\Delta)}L_{J0}, \tag{9}$$

where J is the Bessel function of the first kind. The idea is based on the following considerations: suppose that the superconducting phase δ of JJ is oscillating as

$$\delta = \Delta \sin \omega t. \tag{10}$$

Then, the voltage V_J across the junction and the current I_J through the junction are given by

$$V_J/\varphi_0 = d\delta/dt = \Delta\omega \cos \omega t, \tag{11}$$

and

$$I_J/I_0 = \sin \delta = \sin(\Delta \sin \omega t) = 2\sum_{k=0}^{\infty} J_{2k+1}(\Delta)\sin[(2k+1)\omega t]. \tag{12}$$

Here, let us retain the terms with the first harmonic only, as Manucharyan *et al.*[18] did for solving the Duffing equation. Then, Eq. (12) reduces to

$$I_J/I_0 = 2J_1(\Delta)\sin \omega t. \tag{13}$$

By comparing Eqs. (11) and (13) with the equations for a usual inductor L, $V_L \propto \omega L \cos \omega t$ when $I_L \propto \sin \omega t$, we obtain Eq. (9). Note that L_J is *nonlinear* in the sense that it depends on Δ. Its impedance Z_J, on the other hand, is written as

$$Z_J = j\omega L_J, \tag{14}$$

as if it were a usual *linear* inductor because we retained the terms with the first harmonic only.

Equations (9) and (14) make the simulation easy. Now, for example, it is straightforward to include in the calculations, if necessary, the junction capacitance C_J and the quasiparticle resistance R_{qp}, both of which are parallel to L_J. The relationship between R_{qp} and the quality factors will be discussed in Sec. V. We used the transmission (*ABCD*) matrix (see, for example, Sec. 5.5 of Ref. 19) for the simulation. The matrix T_Z for an impedance Z is

$$T_Z = \begin{pmatrix} 1 & Z \\ 0 & 1 \end{pmatrix}, \tag{15}$$

and that for a section of lossless CPW with a length l is

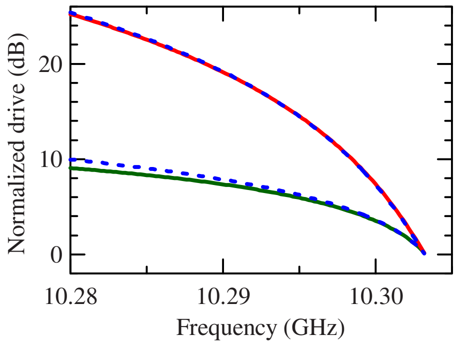

FIG. 2. (Color online) Theoretical boundaries of the bistable region for a nonlinear resonator. The solid and broken curves are the simulation and Eq. (6), respectively.

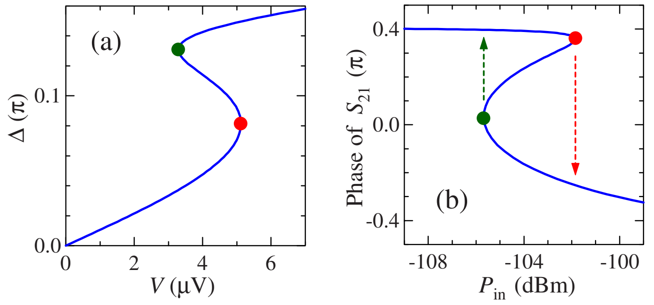

FIG. 3. (Color online) Simulated drive dependence for the resonator in Fig. 2 at $f=10.30$ GHz. (a) Amplitude of the superconducting-phase oscillation [see Eq. (10)] vs drive voltage amplitude. (b) Phase of the transmission coefficient S_{21} vs incident power to the resonator. The markers in both (a) and (b) correspond to the boundaries in Fig. 2. The arrows in (b) indicate the expected switching in actual measurements.

$$T_{\rm cpw} = \begin{pmatrix} \cos \beta l & jZ_{\rm cpw} \sin \beta l \\ j(Z_{\rm cpw})^{-1} \sin \beta l & \cos \beta l \end{pmatrix}, \tag{16}$$

where j is the imaginary unit, $Z_{\rm cpw}$ is the characteristic impedance, $\beta=\omega/v_p$, and v_p is the phase velocity. When CPW has a loss, β in Eq. (16) is replaced by $(\alpha+j\beta)/j$, where α characterizes the loss.

An example of the simulation is shown in Fig. 2. It is for a resonator of the Fig. 1(a) type. The parameters are $I_0=5$ μA, $l=2.8$ mm, and $C_{\rm in}=C_{\rm out}=C_c=5$ fF. Both CPWs are lossless with $Z_{\rm cpw}=50$ Ω and $v_p=0.4c$, where c is the speed of light. When we neglected C_J and assumed that $R_{\rm qp}^{-1}=0$, the simulation yielded $f_0 \equiv \omega_0/(2\pi)=10.306$ GHz, $Q_l=Q_e=3.0\times 10^3$, and $V_c=2.2$ μV. This simulated V_c and the value calculated from Eqs. (1), (7), and (8) agree within 2%. In Fig. 2, the solid curves are the simulated boundaries of the bistable region, and compared with Eq. (6), the broken curves. The vertical axis of Fig. 2 is the drive voltage amplitude V normalized by V_c. In general, the solid and broken curves are similar. As the drive amplitude is increased, the difference becomes visible especially for the lower boundary, but this trend should be reasonable because the mapping of Eqs. (7) and (8) is based on the behavior in the linear regime as we mentioned earlier, and because at a given frequency, Δ at the lower boundary is actually larger than Δ at the upper boundary as we will see in Fig. 3(a).

The simulated boundaries in Fig. 2 were obtained by calculating Δ vs V at different frequencies. Such calculation for $f=10.30$ GHz is shown in Fig. 3(a); the marked local maximum and minimum of V are the boundaries. In experiments, we measure instead of Δ, the transmission coefficient S_{21} of $\lambda/2$ resonators and the reflection coefficient Γ of $\lambda/4$ resonators. These quantities are also simulated by the same method. The phase of S_{21} is computed in Fig. 3(b) as a function of the incident power $P_{\rm in}$, which is more relevant than V from the experimental point of view. The power is given by

$$P_{\rm in} = V_{\rm in}^2/(2Z_0), \tag{17}$$

where

$$V_{\rm in} = V/2 \tag{18}$$

is the amplitude of the incident voltage. Because the section between the markers is unstable, the resonator response in actual measurements is expected to be hysteretic, that is, switching indicated by the arrows in Fig. 3(b) should be observed.

Regarding $\lambda/4$ resonators, when we chose in Fig. 1(b), $I_0'=2I_0$, $C_c'=C_c$, $l'=l$, and the same unit-length CPW properties, the simulation yielded essentially the same ω_0, Q_l, V_c, etc., as those of the $\lambda/2$ resonator in Figs. 2 and 3.

When we compare the theoretical predictions in this section with experimental results, we should note that in experiments, we cannot make the drive amplitude arbitrarily large in order to see the bistability arising from the nonlinear inductance of JJs because, for example, I_J has to be smaller than I_0. Let us also recall that both Eq. (6) and the simulation are based on the approximation of retaining the terms with the first harmonic only; the accuracy of the approximation becomes worse as the drive amplitude increases.

III. EXPERIMENT

We studied two series of CPW resonators listed in Table I. The fabrication of Series A, which has single JJs, was almost the same as that of the sample in Ref. 12; a Si wafer covered by a layer of thermally oxidized SiO_2 was used, Nb inter-

TABLE I. List of resonators. A1–A4 have single Josephson junctions whereas B1–B2 have dc SQUIDs. f_0 is the resonant frequency in the linear regime, Q_l is the loaded quality factor, and P_c is the critical incident power for the bifurcation. All values are for the zero magnetic field and Q_l was calculated in the linear regime.

Resonator	Type	f_0 (GHz)	Q_l ($\times 10^3$)	P_c (dBm)
A1	$\lambda/2$	9.86	6	-97 ± 2
A2	$\lambda/4$	9.70	3	-100 ± 1
A3	$\lambda/2$	9.98	1.1	-101 ± 2
A4	$\lambda/4$	9.83	1.6	-103 ± 3
B1	$\lambda/2$	11.30	1.0	-85 ± 1
B2	$\lambda/4$	11.12	1.3	-82 ± 1

digital coupling capacitors and Nb CPWs were patterned by photolithography and reactive ion etching, and Al JJs by electron-beam lithography and shadow evaporation. In order to realize a superconducting contact between Nb and Al, the surface of Nb was cleaned by Ar^+ milling before the Al evaporation. In Series B with dc SQUIDs, on the other hand, all electrodes including those of SQUIDs are Nb, and everything was fabricated by the photolithographic technology. Thus, between the two series of resonators, there are a couple of differences regarding the CPW that we should note: the thickness of Nb film and the quality of SiO_2.

The Nb film is much thinner in Series A (0.05 μm) than in Series B (0.4 μm). As a result, highly likely due to the kinetic inductance,[20] we saw a noticeable difference in v_p. In Series A, Nb is deposited directly on the thermally oxidized SiO_2 of the Si wafer, whereas in Series B, there is a layer of sputtered SiO_2 between Nb and thermally oxidized SiO_2. It seems that this sputtered SiO_2 decreases Q_u. According to Ref. 21, the loss tangent of SiO_2 grown by plasma-enhanced chemical-vapor deposition is much larger than that of thermally oxidized SiO_2. Thus, it is highly likely that sputtered SiO_2 is also much more lossy than thermally oxidized SiO_2. We will come back to this point in Sec. IV B.

Our $\lambda/2$ resonators (A1, A3, and B1) are designed to be symmetric, that is, in Fig. 1(a), $C_{\mathrm{in}}=C_{\mathrm{out}}=C_c$ and the two CPWs are the same. For all resonators, we intended to obtain $f_0\sim 10$ GHz and Q_l on the order of 10^3 with l, $l'\sim 3$ mm, by aiming at I_0, $I_0'\sim 3-30$ μA, $Z_{\mathrm{cpw}}\sim 50$ Ω, $v_p\sim 0.4c$, and C_c, $C_c'\sim 2-10$ fF.

The resonators were characterized in a $^3\mathrm{He}$-$^4\mathrm{He}$ dilution refrigerator at the base temperature, $T<0.05$ K. For the characterization, we used a vector network analyzer choosing an intermediate frequency (IF) between 100 Hz and 40 kHz. The transmission coefficient S_{21} of $\lambda/2$ resonators were measured by connecting Ports 1 and 2 in Fig. 1(a) to the network analyzer. In the input microwave line connected to Port 1, 20 dB attenuators were inserted at $T=1$ K and at the base temperature. The output line had an isolator at $T=1$ K, and at $T=4$ K, an cryogenic amplifier, whose gain at 10–11 GHz was 34–38 or 40 dB. For measuring the reflection coefficient Γ of $\lambda/4$ resonators, we employed a directional coupler and extra isolators at the base temperature as in Fig. 1(a) of Ref. 12. Magnetic fields were applied in the direction perpendicular to the substrate by means of a superconducting solenoid.

The gains of amplifiers and the insertion losses of attenuators and cables had been characterized at relevant frequencies by independent measurements. The uncertainties of P_{in}, $|S_{21}|$, and $|\Gamma|$ in this paper are less than 1–2 dB.

IV. RESULTS

Basic parameters of the resonators are listed in Table I. We obtained $f_0\sim 10$ GHz and Q_l on the order of 10^3 as we designed. Hystereses were observed in all resonators; the critical incident power P_c in Table I was determined experimentally. The values of $P_c[=(V_c/2)^2/(2Z_0)]$ for Series A correspond to I_0, $I_0'=5-21$ μA, or the critical-current density $J_c=1-2$ kA/cm^2, within the theory[18] and the mapping[10,11] in Sec. II. The estimated critical current is on the right order of magnitude and consistent with the dc measurements on test junctions fabricated on the same wafer, $J_c\sim 1$ kA/cm^2. We also estimated the critical current by the simulation in Sec. II taking into account the junction capacitance and confirmed that the estimates did not change significantly. The situation is similar in Series B. The estimated $J_c=0.5-0.6$ kA/cm^2 is on the right order of magnitude, and consistent with the parameters of the fabrication process, which targeted at $J_c=0.4$ kA/cm^2. Below, we focus on Resonators A1 and B1 because within each series, the results were qualitatively similar.

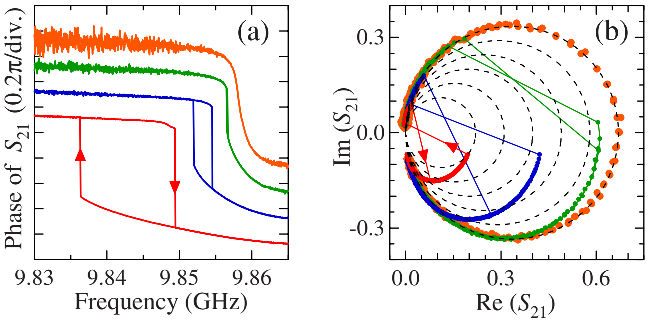

FIG. 4. (Color online) Dependence on the incident power P_{in} of Resonator A1. In both (a) and (b), from right to left, $P_{\mathrm{in}}=-101$, -93, -85, and -75 dBm. (a) Phase of the transmission coefficient S_{21} vs frequency. The frequency is swept up and down for all curves. For the $P_{\mathrm{in}}=-75$ dBm curve, the sweep directions are indicated by the arrows. The origin of the vertical axis is offset for each curve for clarity. (b) Imaginary part of S_{21} vs real part of S_{21}. The diameters d of the dotted circles range from 0.22 to 0.67 in steps of 0.09. The centers are located at $(d/2,0)$.

A. Resonator with a single Josephson junction

The P_{in} dependence of Resonator A1 is shown in Fig. 4. At different values of P_{in}, the frequency f was swept up and down while S_{21} was recorded. At $P_{\mathrm{in}}=-101$ dBm$<P_c$, that is, in the linear regime, the phase of S_{21} vs f shows a usual rotation [the top right curve in Fig. 4(a)], and the polar plot of $\mathrm{Im}(S_{21})$ vs $\mathrm{Re}(S_{21})$ falls on the largest dotted circle in Fig. 4(b). The center of the circle is at $(d/2,0)$, where $d(=0.67)$ is the diameter. Note that d is equal to the maximum $|S_{21}|$. It is also related to the quality factors by

$$Q_e/Q_u=d^{-1}-1. \tag{19}$$

Thus, $Q_e/Q_u=0.5$ for Resonator A1 in the linear regime. The other curves in Fig. 4 are for $P_{\mathrm{in}}>P_c$, and hysteresis is seen as the theory predicts. An interesting feature in Fig. 4(b) is that the three curves for $P_{\mathrm{in}}>P_c$ do not always stay on the largest circle. They move toward smaller circles as $|S_{21}|$ increases and the trend is stronger at larger P_{in}. This P_{in}-dependent quality factors are a key to understand Fig. 5, where the measured bistable region in gray is compared with Eq. (6).

The gray area in Fig. 5 is determined from many two-directional frequency sweeps like Fig. 4(a). If the phase difference of S_{21} between up and down frequency sweeps at (f,P_{in}) was more than 0.1π, (f,P_{in}) in Fig. 5 is gray. The

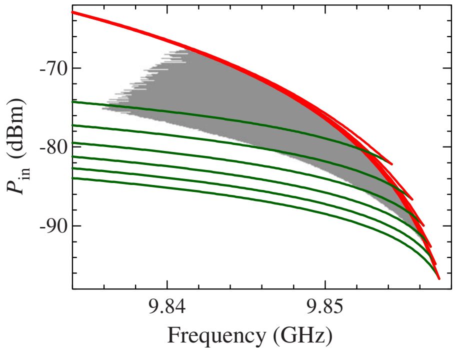

FIG. 5. (Color online) Bistable region (gray) of Resonator A1. The pairs of curves are, Eq. (6), with different loaded quality factors Q_l. As the power $P_{\rm in}$ is increased, the theoretical curves with a smaller Q_l reproduce the experimental bistable region.

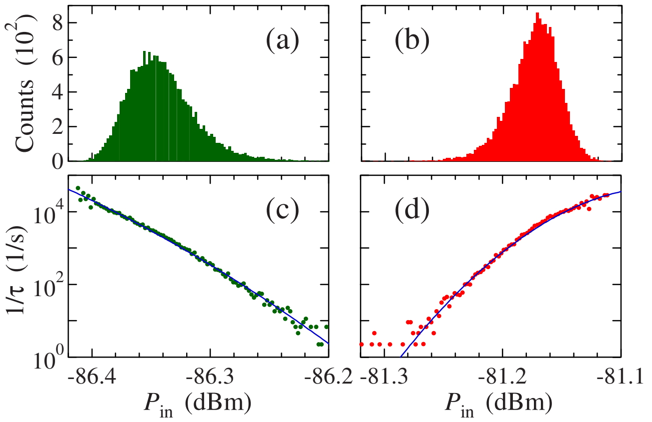

FIG. 6. (Color online) Switching between the bistable states at f=9.853 GHz in Resonator A1. [(a) and (b)] Histograms of the switching events. The horizontal axis is the incident power $P_{\rm in}$. [(c) and (d)] Inverse of τ vs $P_{\rm in}$, where τ is the lifetime of the bistable state calculated from (a) and (b), respectively. The curves are the least-squares fittings of Eqs. (20) and (21).

pairs of curves in Fig. 5 are, Eq. (6), with different values of Q_l. The pair with the largest ω_c is for $Q_l = Q_{l0}$ in the linear regime and associated with the largest circle in Fig. 4(b). The other pairs in Fig. 5 correspond to the smaller circles in Fig. 4(b) when we neglect the $P_{\rm in}$ dependence of Q_e, which is expected to be much smaller than that of d in Resonator A1. The ratio of $V_c(Q_l)/V_c(Q_{l0})$ in Fig. 5 is consistent with Eqs. (1) and (5), that is, the ratio is equal to $(Q_l/Q_{l0})^{-3/2}(1-\sqrt{3}/Q_l)/(1-\sqrt{3}/Q_{l0})$. We treated $V_c(Q_{l0})$ as an adjustable parameter and chose its value so that the experimental bistable region stayed between the theoretical boundaries.

The theoretical size of the bistable region in Fig. 5 shrinks rapidly with decreasing Q_l, and as we have seen, Fig. 4(b) suggests that Q_l of the resonator decreases with increasing $P_{\rm in}$ especially around the lower boundary, where $|S_{21}|$ takes the maximum value. Thus, $P_{\rm in}$-dependent Q_l should mostly explain the fact that the experimental bistable region is considerably smaller than the theoretical prediction for $Q_l = Q_{l0}$. In general, the size of experimentally determined bistable region may depend on the sweep speed due to finite lifetimes of the bistable states. This effect, however, seems to be not significant in Fig. 5 judging from the experiment described in the following paragraphs.

We swept $P_{\rm in}$ instead of f in two directions with IF = 40 kHz, which is much faster than IF = 200 Hz in Fig. 5. We chose f=9.848 and 9.853 GHz, where the widths of the bistable region in Fig. 5 are 8.1 and 5.2 dB, respectively. At both frequencies, the values of $P_{\rm in}$ at which the phase of S_{21} switched [see also the arrows in Fig. 3(b)] agreed with Fig. 5 within 0.1 dB, despite the large difference in the sweep speed. This is the main reason why we presume that the dependence on the sweep speed is insignificant in Fig. 5.

At f=9.853 GHz, the measurements were repeated 1.8×10^4 times and the histograms of the switching events are shown in Figs. 6(a) and 6(b). The distribution widths of the switching events are much smaller than the width of the bistable region. The histograms can be converted to the lifetimes τ of the bistable states by assuming that the probability of remaining in the same state decays as $\exp(-\Delta t/\tau)$, where Δt is the time and in our case, equal to the inverse of IF. This type of conversion has been done many times for the conventional switching from the zero-voltage state to the voltage state in JJs, and the details of the conversion are found, for example, in Ref. 22. The lifetimes obtained from Figs. 6(a) and 6(b) are shown in Figs. 6(c) and 6(d), respectively. Below, we analyze τ within a simple model.

Let us suppose that

$$\tau^{-1} \propto \exp(-E/k_B T) \tag{20}$$

and that as in Ref. 23, E is associated with the noise. When we further assume for simplicity that E is proportional to the minimum V_N^2, where V_N is the noise voltage satisfying $V_N + Ve^{j\theta_N} = V_b$, V is the source voltage, θ_N is the phase noise, and V_b corresponds to one of the theoretical boundaries of the bistable region [see the markers in Fig. 3(a)], the power dependence of E is written as

$$E \propto (\sqrt{P_{\rm in}} - \sqrt{P_b})^2 \tag{21}$$

because V and V_b are in phase when V_N^2 takes the minimum value. Intuitively speaking, the switching between the bistable states would occur at P_b if an experiment with no noise were possible. The last assumption is actually consistent with the approach based on the Poincaré section in Fig. 2 of Ref. 2 because the height of the saddle point in the Poincaré section is proportional to the minimum $|V_N|$.

The curves in Figs. 6(c) and 6(d) are the least-squares fittings of Eqs. (20) and (21). The fittings yielded $P_b = P_l - 0.5$ dB and $P_h + 0.1$ dB. Because P_b extends the bistable region by 0.6 dB only in total, the above analysis of τ at f = 9.853 GHz supports our presumption that the dependence on the sweep speed is insignificant in Fig. 5.

B. Resonator with a dc SQUID

The SQUID modulation of Resonator B1 in the linear regime measured at $P_{\rm in}$=−113 dBm is shown in Fig. 7. The external dc magnetic flux Φ indeed changes I_0, and thereby, L_{J0} and f_0, periodically. Around $\Phi/\Phi_0 = \pm 0.5$, the response was a little hysteretic and f_0 depended on the direction of the

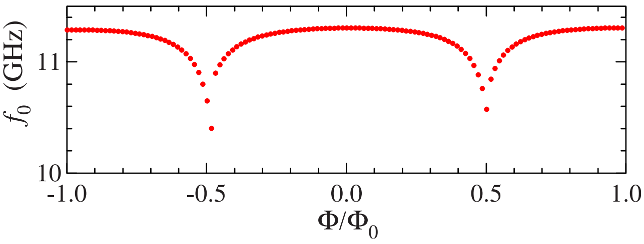

FIG. 7. (Color online) Resonant frequency f_0 in the linear regime vs external dc magnetic flux Φ normalized by the superconducting flux quantum $\Phi_0 = h/(2e)$ for Resonator B1. The direction of the flux sweep was from left to right.

flux sweep. In Fig. 7, the flux was swept in one direction only, and that is why there is small asymmetry at $\Phi/\Phi_0 \sim \pm 0.5$. From the amplitude of the f_0 modulation, we estimate based on the simulation in Sec. II that at $\Phi/\Phi_0 \sim \pm 0.5$, the critical current of the SQUID becomes about 15% of its maximum value, and thus, the SQUID has a normalized loop inductance of $L_{\rm SQ} I_{00}/\Phi_0 \sim 0.1$, where I_{00} is the critical current per junction at $\Phi = 0$. The above value of $L_{\rm SQ} I_{00}/\Phi_0$ is consistent with the design.

For different values of f_0, we measured the bistable regions. Some of the results are shown in Fig. 8. The rightmost data set was obtained when f_0 was close to its maximum value. Regarding quality factors, we found two major differences compared to Resonator A1. One is that $Q_e/Q_u(\sim 5)$ in the linear regime is much larger. This should be due to the layer of sputtered $\mathrm{SiO_2}$ that exists only in Series B as we mentioned in Sec. III. The other difference is that judging from polar plots (data not shown) like Fig. 4(b), Q_l does not change very much when $P_{\rm in}$ is increased from P_c. Actually, we estimate at $P_{\rm in} \sim P_c$, a larger value of $Q_l = 1.3 \times 10^3$ than that in the linear regime. The two curves for the rightmost data set in Fig. 8 are, Eq. (6), calculated with $Q_l = 1.3 \times 10^3$. They reproduce the experimental boundaries of the bistable region.

The other data sets in Fig. 8 for smaller values of f_0 are also compared with Eq. (6), where we employed for Q_l, the estimated values at $P_{\rm in} \sim P_c$ again. The dependence of P_c on f_0 qualitatively agrees with Eq. (1) because a smaller f_0 means a larger L_{J0}. As f_0 is decreased, however, it becomes easier to see some discrepancies between the experimental boundaries and Eq. (6). In the leftmost data set, for example, polar plots (data not shown) like Fig. 4(b) suggest a moderate decrease in Q_l with increasing $P_{\rm in}$ above $P_{\rm in} \sim P_c$. Qualitatively speaking, the behavior of Q_l is becoming similar to that in Resonator A1.

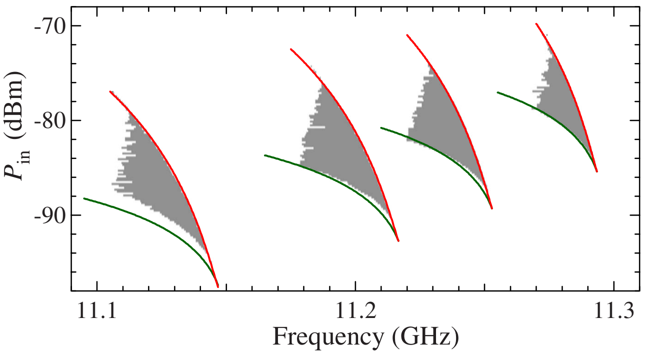

FIG. 8. (Color online) Bistable regions (gray) of Resonator B1 when the resonant frequencies f_0 in the linear regime were tuned to 11.16, 11.23, 11.26, and 11.30 GHz by dc magnetic flux. The pairs of curves are, Eq. (6), where the loaded quality factors from left to right are $Q_l/10^3 = 1.2$, 1.2, 1.2, and 1.3.

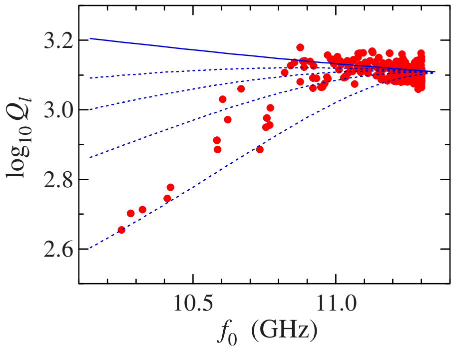

FIG. 9. (Color online) Logarithm of the loaded quality factor Q_l as a function of the resonant frequency f_0 in the linear regime for Resonator B1. The solid and dotted curves are the theoretical predictions based on the simulation in Sec. II. The solid curve is for $R_{\rm qp}^{-1} = 0$, that is, the quasiparticle resistance $R_{\rm qp}$ of the SQUID is not taken into account, whereas the dotted curves from top to bottom are for $R_{\rm qp} = 20$, 10, 5, and 2 kΩ, respectively.

When f_0 is decreased further down to $f_0 < 11$ GHz, we did not find the bistable region at all, which is a bit surprising because according to Eq. (2), a larger L_{J0} is more advantageous for observing the bistability, in principle. We should not forget, however, that I_c/I_0 in Eq. (2) depends on Q_l as well, and in fact, Q_l at $f_0 < 11$ GHz decreases with decreasing f_0 rather sharply even in the linear regime as shown in Fig. 9, where the vertical axis is the logarithm of Q_l, and Q_l was calculated from the data at $P_{\rm in} = -113$ dBm. We will discuss the origin of the change in Q_l later in the next section. The lifetimes τ of the bistable states may be also related to the disappearance of the bistable region at $f_0 < 11$ GHz. As f_0 is decreased, the relevant power range becomes smaller. Within the simple model of Eqs. (20) and (21), smaller $P_{\rm in}$ and P_b make E smaller, and thereby, τ shorter. Thus, we cannot exclude the possibility that our measurements were not fast enough for observing the bistability at $f_0 < 11$ GHz.

V. DISCUSSION

In the preceding section, we have seen that how the quality factor depends on $P_{\rm in}$ or Φ is relevant to the experimental bistable region. In this section, let us discuss the origin of the dependence.

Experimental determination of all the quality factors in Eq. (3) is straightforward in the linear regime. For $\lambda/2$ resonators, Q_l is obtained from $|S_{21}|$ vs f and Q_e/Q_u from Eq. (19) by substituting the maximum value of $|S_{21}|$ for d. In Fig. 9, for example, the sharp decrease in Q_l at $f_0 < 11$ GHz is mostly due to the change in Q_u. We have also confirmed that the frequency dependence of Q_e is consistent with the theoretical prediction that Q_e is determined mainly by $\omega_0 C_c$. The unloaded quality factor Q_u is a measure of the internal loss. In our resonators, both CPWs and JJs can be the source of loss. Resonators A1 and B1 have completely different Q_u in the linear regime: $Q_u = 1.6 \times 10^4$ and 1.3×10^3, respectively. As the most probable reason, we have already mentioned the difference in the quality of the dielectric for the CPWs. The value of $Q_u = 1.6 \times 10^4$ for Resonators A1 is actually still considerably smaller than those we obtained for usual CPW resonators without JJ fabricated at the same time as Resonators A1. Thus, there should be a contribution from JJ as well.

In the bistable region, it is still possible to estimate the quality factors. We have seen that Fig. 4(b) suggests a strong P_{in} dependence of Q_u in Resonator A1. The P_{in} dependence is likely to be due to a finite R_{qp} of JJ. The main reason is that the usual CPW resonators without JJ looked almost P_{in} independent in the relevant power range. In general, Q_u of CPW resonators is known to increase with increasing P_{in} at least in the weak-power range, where the average energy stored in the resonator at ω_0 is comparable to $\hbar\omega_0$ or smaller.[21] This behavior was also observed in our resonators in the linear regime. Both in Resonators A1 and B1, Q_u gained several percents when P_{in} was increased by 5 dB from $P_c - 15$ dBm. Figure 4(b) is explained if R_{qp} is a function of V_J and its value decreases with increasing V_J, which is quite likely (see, for example, Sec. 6.3 of Ref. 24). Although we are interested in the case that the JJ stays in the superconducting branch with zero dc voltage, it does not necessarily mean that the ac voltage is also zero. The ac voltage is given by Eq. (11), and when it is nonzero, an ac current flows through R_{qp} causing a loss. This picture is supported by the following quantitative consideration: according to the simulation in Sec. II, the reduction in Q_l becomes considerable when R_{qp} is decreased below $10^3\ \Omega$ in Resonator A1, whereas the dc measurements on the test junctions suggest that R_{qp} in Resonator A1 can be as low as $3 \times 10^2\ \Omega$. It is also consistent with the results on Resonator B1. Because B1 has a smaller J_c and a much larger superconducting gap, the tunnel barrier of the junctions is thicker. Thus, R_{qp} must be much larger, which explains the fact that P_{in} dependence is much smaller. The Φ dependence is also explained because Φ modulates the ratio of $R_{\mathrm{qp}}/(\omega_0 L_{J0})$. As Φ approaches $\pm 0.5\Phi_0, \pm 1.5\Phi_0, \ldots$, L_{J0} increases, but there is no obvious mechanism that Φ changes R_{qp}. We have also confirmed by the simulation in Sec. II that Q_l indeed depends on the ratio of $R_{\mathrm{qp}}/(\omega_0 L_{J0})$, and that the experimental Q_l vs f_0 in Fig. 9 is qualitatively reproduced with R_{qp} on the order of $10^3 - 10^4\ \Omega$. In Fig. 9, the predictions based on the simulation for different values of R_{qp} are also shown by the solid and dotted curves.

From the viewpoint of the qubit readout and the qubit coherence time, the dissipation due to the loss at R_{qp} can be unfavorable depending on the circuit configuration, and worse than that at CPWs when R_{qp} is closer to the qubit. Fortunately, now we know from the experiment in Sec. IV, how large R_{qp} has to be in order for the loss at R_{qp} to be negligible. For our resonators in Table I, the ratio of $R_{\mathrm{qp}}/(\omega_0 L_{J0})$ needs to be larger than $10^3 - 10^4$ according to the simulation in Sec. II. This condition should be easily satisfied even with Al JJs by employing a sufficiently small critical-current density J_c.

VI. CONCLUSION

We studied nonlinear superconducting resonators with single Josephson junctions or dc SQUIDs. The bistable region of the resonators were experimentally determined and compared with the theory and simulations. We found that the variation in the unloaded quality factor as a function of relevant quantities such as the drive power and the external magnetic flux was important for understanding the experimental results. The unloaded quality factor is a measure of the internal loss and the origin of its variation was also discussed.

ACKNOWLEDGMENTS

The authors thank Y. Nakamura for comments, K. Matsuba for across-the-board assistance, and Y. Kitagawa for fabrication assistance. M.W. thanks R. L. Kautz for fruitful discussion. T.Y. and J.-S.T. thank CREST-JST, Japan for financial support.

---

*Present address: Fort Lupton Fire Protection District, 1121 Denver Avenue, Fort Lupton, Colorado 80621, U.S.A.

[1] A. Wallraff, D. I. Schuster, A. Blais, L. Frunzio, J. Majer, M. H. Devoret, S. M. Girvin, and R. J. Schoelkopf, Phys. Rev. Lett. **95**, 060501 (2005).

[2] I. Siddiqi, R. Vijay, F. Pierre, C. M. Wilson, M. Metcalfe, C. Rigetti, L. Frunzio, and M. H. Devoret, Phys. Rev. Lett. **93**, 207002 (2004).

[3] I. Siddiqi, R. Vijay, M. Metcalfe, E. Boaknin, L. Frunzio, R. J. Schoelkopf, and M. H. Devoret, Phys. Rev. B **73**, 054510 (2006).

[4] N. Boulant, G. Ithier, P. Meeson, F. Nguyen, D. Vion, D. Esteve, I. Siddiqi, R. Vijay, C. Rigetti, F. Pierre, and M. Devoret, Phys. Rev. B **76**, 014525 (2007).

[5] M. B. Metcalfe, E. Boaknin, V. Manucharyan, R. Vijay, I. Siddiqi, C. Rigetti, L. Frunzio, R. J. Schoelkopf, and M. H. Devoret, Phys. Rev. B **76**, 174516 (2007).

[6] A. Lupaşcu, C. J. M. Verwijs, R. N. Schouten, C. J. P. M. Harmans, and J. E. Mooij, Phys. Rev. Lett. **93**, 177006 (2004).

[7] A. Lupaşcu, E. F. C. Driessen, L. Roschier, C. J. P. M. Harmans, and J. E. Mooij, Phys. Rev. Lett. **96**, 127003 (2006).

[8] J. C. Lee, W. D. Oliver, K. K. Berggren, and T. P. Orlando, Phys. Rev. B **75**, 144505 (2007).

[9] A. Lupaşcu, S. Saito, T. P. P. C. de Groot, C. J. P. M. Harmans, and J. E. Mooij, Nat. Phys. **3**, 119 (2007).

[10] E. Boaknin, V. E. Manucharyan, S. Fissette, M. Metcalfe, L. Frunzio, R. Vijay, I. Siddiqi, A. W. R. J. Schoelkopf, and M. Devoret, arXiv:cond-mat/0702445 (unpublished).

[11] O. Naaman, J. Aumentado, L. Friedland, J. S. Wurtele, and I. Siddiqi, Phys. Rev. Lett. **101**, 117005 (2008).

[12] K. Inomata, M. Watanabe, T. Yamamoto, K. Matsuba, Y. Nakamura, and J. S. Tsai, J. Phys.: Conf. Ser. **150**, 052077 (2009).

[13] P. Bertet, I. Chiorescu, G. Burkard, K. Semba, C. J. P. M. Harmans, D. P. DiVincenzo, and J. E. Mooij, Phys. Rev. Lett. **95**, 257002 (2005).

[14] A. A. Houck, J. A. Schreier, B. R. Johnson, J. M. Chow, J. Koch, J. M. Gambetta, D. I. Schuster, L. Frunzio, M. H. Devoret, S. M. Girvin, and R. J. Schoelkopf, Phys. Rev. Lett. **101**, 080502 (2008).

[15] C. C. Chin, D. E. Oates, G. Dresselhaus, and M. S. Dresselhaus, Phys. Rev. B **45**, 4788 (1992).

[16] Z. Ma, E. de Obaldia, G. Hampel, P. Polakos, P. Mankiewich, B. Batlogg, W. Prusseit, H. Kinder, A. Anderson, D. E. Oates *et al.*, IEEE Trans. Appl. Supercond. **7**, 1911 (1997).

[17] E. A. Tholén, A. Ergül, E. M. Doherty, F. M. Weber, F. Grégis, and D. B. Haviland, Appl. Phys. Lett. **90**, 253509 (2007).

[18] V. E. Manucharyan, E. Boaknin, M. Metcalfe, R. Vijay, I. Siddiqi, and M. Devoret, Phys. Rev. B **76**, 014524 (2007).

[19] D. M. Pozar, *Microwave Engineering* (Addison-Wesley, Reading, Massachusetts, 1990).

[20] R. Meservey and P. M. Tedrow, J. Appl. Phys. **40**, 2028 (1969).

[21] A. D. O'Connell, M. Ansmann, R. C. Bialczak, M. Hofheinz, N. Katz, E. Lucero, C. McKenney, M. Neeley, H. Wang, E. M. Weig, A. N. Cleland, and J. M. Martinis, Appl. Phys. Lett. **92**, 112903 (2008).

[22] T. A. Fulton and L. N. Dunkleberger, Phys. Rev. B **9**, 4760 (1974).

[23] R. L. Kautz, Phys. Rev. A **38**, 2066 (1988).

[24] M. Tinkham, *Introduction to Superconductivity*, 2nd ed. (McGraw-Hill, New York, 1996).